Magnetic properties of ilmenite-hematite single crystals from the Ecstall pluton near Prince Rupert, British Columbia

Brownlee, Sarah J.; Feinberg, Joshua M.; Kasama, Takeshi; Harrison, Richard J.; Scott, Gary R.; Renne, Paul R.

Published in:
G3: Geochemistry, Geophysics, Geosystems

Link to article, DOI:
10.1029/2011GC003622

Publication date:
2011

Document Version
Publisher's PDF, also known as Version of record

Geochemistry Geophysics Geosystems G3

Article
Volume 12, Number 9
10 September 2011
Q07Z29, doi:10.1029/2011GC003622
ISSN: 1525-2027

Published by AGU and the Geochemical Society

Magnetic properties of ilmenite-hematite single crystals from the Ecstall pluton near Prince Rupert, British Columbia

Sarah J. Brownlee
Department of Earth and Planetary Science, University of California, 307 McCone Hall, Berkeley, California 94720, USA

Now at Earth Research Institute, University of California, 6832 Ellison Hall, Santa Barbara, California 93106-3060, USA (brownlee.sj@gmail.com)

Joshua M. Feinberg
Institute for Rock Magnetism, University of Minnesota, 310 Pillsbury Drive SE, Minneapolis, Minnesota 55455, USA

Takeshi Kasama
Center for Electron Nanoscopy, Technical University of Denmark, DK-2800 Kongens Lyngby, Denmark

Richard J. Harrison
Department of Earth Sciences, University of Cambridge, Downing Street, Cambridge CB2 3EQ, UK

Gary R. Scott
Berkeley Geochronology Center, 2455 Ridge Road, Berkeley, California 94709, USA

Paul R. Renne
Department of Earth and Planetary Science, University of California, 307 McCone Hall, Berkeley, California 94720, USA

Berkeley Geochronology Center, 2455 Ridge Road, Berkeley, California 94709, USA

[1] Paleomagnetic studies of the 91 Ma Ecstall pluton and other Cretaceous plutons of British Columbia imply large northward tectonic movements (>2000 km) may have occurred during the tectonic evolution of western North America. However, more recent studies have shown that the eastern edge of the Ecstall pluton experienced considerable mineralogical changes as younger Eocene plutons, such as the ~58 Ma Quottoon Pluton, were emplaced along its margins. We investigated changes in the rock magnetic properties associated with this reheating event by examining isolated grains of intergrown ilmenite and hematite, the primary paleomagnetic recorder in the Ecstall pluton. Measurements of hysteresis properties, low-temperature remanence, and room temperature isothermal remanent magnetization acquisition and observations from magnetic force microscopy and off-axis electron holography indicate that samples fall into three groups. The groups are defined by the presence of mineral microstructures that are related to distance from the Quotoon plutonic complex. The two groups closest to the Quottoon Pluton contain magnetite within hematite and ilmenite lamellae. Reheating of the Ecstall pluton led to an increase in coercivity and magnetization, as well as to development of mixed phase hysteresis. These results indicate that shallow paleomagnetic directions from the western Ecstall pluton are not affected by reheating and are therefore likely to record original field conditions at the time of pluton emplacement. In the absence of structural deformation, these shallow inclinations are consistent with large-scale northward translation suggested by the Baja–British Columbia hypothesis.

Components: 8200 words, 9 figures, 2 tables.

Keywords: Baja-BC; IRM acquisition; hysteresis; low-temperature remanence; magnetic force microscopy; off-axis electron holography.

Index Terms: 1519 Geomagnetism and Paleomagnetism: Magnetic mineralogy and petrology; 1533 Geomagnetism and Paleomagnetism: Remagnetization; 1540 Geomagnetism and Paleomagnetism: Rock and mineral magnetism.

Received 10 March 2011; **Revised** 13 June 2011; **Accepted** 13 June 2011; **Published** 10 September 2011.

Brownlee, S. J., J. M. Feinberg, T. Kasama, R. J. Harrison, G. R. Scott, and P. R. Renne (2011), Magnetic properties of ilmenite-hematite single crystals from the Ecstall pluton near Prince Rupert, British Columbia, *Geochem. Geophys. Geosyst.*, *12*, Q07Z29, doi:10.1029/2011GC003622.

Theme: Magnetism from Atomic to Planetary Scales: Physical Principles and Interdisciplinary Applications in Geoscience

1. Introduction

[2] Shallow paleomagnetic inclinations from westernmost British Columbia (BC) have generated much debate about the degree of tectonic plate motion along the western edge of the North American craton [*Umhoefer*, 1987; *Wynne et al.*, 1995; *Cowan et al.*, 1997; *Enkin et al.*, 2003]. Variations in paleomagnetic inclinations across the ~91 Ma Ecstall pluton near Prince Rupert, BC have only added to the debate [*Butler et al.*, 2002; *Hollister et al.*, 2004; *Beck and Housen*, 2005]. Inclinations from the Ecstall pluton's western margin are shallow, which indicates that the magnetic remanence was acquired at low latitudes. Proponents of the Baja-BC hypothesis would cite these shallow inclinations as further evidence for large northward translation (>2000 km) of allochthonous terranes. By contrast, inclinations from the Ecstall pluton's eastern margin are steeper and match those observed in plutons emplaced during the Eocene as part of the Coast Mountains Batholith (CMB), which is located immediately east of the Ecstall pluton (Figure 1) [*Butler et al.*, 2002]. These measurements have been interpreted as evidence for substantially reduced northward translation of the Ecstall pluton (<100 km) [*Butler et al.*, 2002]. Determining the cause of the difference in paleomagnetic inclination between the western and eastern margins of the Ecstall pluton is an essential step in refining the tectonic history of western North America.

[3] *Hollister et al.* [2004] proposed that paleomagnetic recording in the eastern portion of the Ecstall pluton was thermally reset during emplacement and uplift of the nearby ~58 Ma Quotoon pluton, the nearest member of the CMB. The thermal overprint of the Quottoon Pluton on the Ecstall and other preexisting plutons is manifest in detailed $^{40}Ar/^{39}Ar$ studies that reveal partial to complete degassing of argon from biotite and hornblende near the contact [*Brownlee and Renne*, 2010]. In a microscopy study of the oxide mineralogy in the Ecstall pluton, *Brownlee et al.* [2010] found that hematite-ilmenite samples closer than ~14 km to the Quottoon Pluton contain magnetite precipitates (20–50 nm) within the hematite lamellae. The origin of this magnetite is thought to be related to changes in temperature and oxygen fugacity associated with reheating of the Ecstall pluton. The presence of this magnetite should exert a profound influence on the magnetic properties of the reheated portion of the pluton.

[4] In this study, we examine the magnetic properties of single crystals of ilmenite-hematite collected along a transect across the full width of the Ecstall pluton. The Fe-Ti oxides in this study are known to contain a range of complex mineral microstructures and we use a combination of geophysical and microscopic techniques to try to link magnetic behaviors to specific microstructures. By understanding how the rock magnetic properties vary across the Ecstall pluton, especially in relation to the thermal boundary associated with the Quottoon Pluton, we hope to shed light on the inclination change across this tectonically important pluton.

2. Methods

[5] Samples are from the same Skeena River transect described by *Brownlee et al.* [2010] (Figure 1). Whole rock samples were crushed and sieved and a magnetic fraction was extracted using a Frantz magnetic separator. Single Fe-Ti oxide grains were picked from the 425–800 μm size fraction. Care was taken to select only those grains with a minimal amount of adhered silicate.

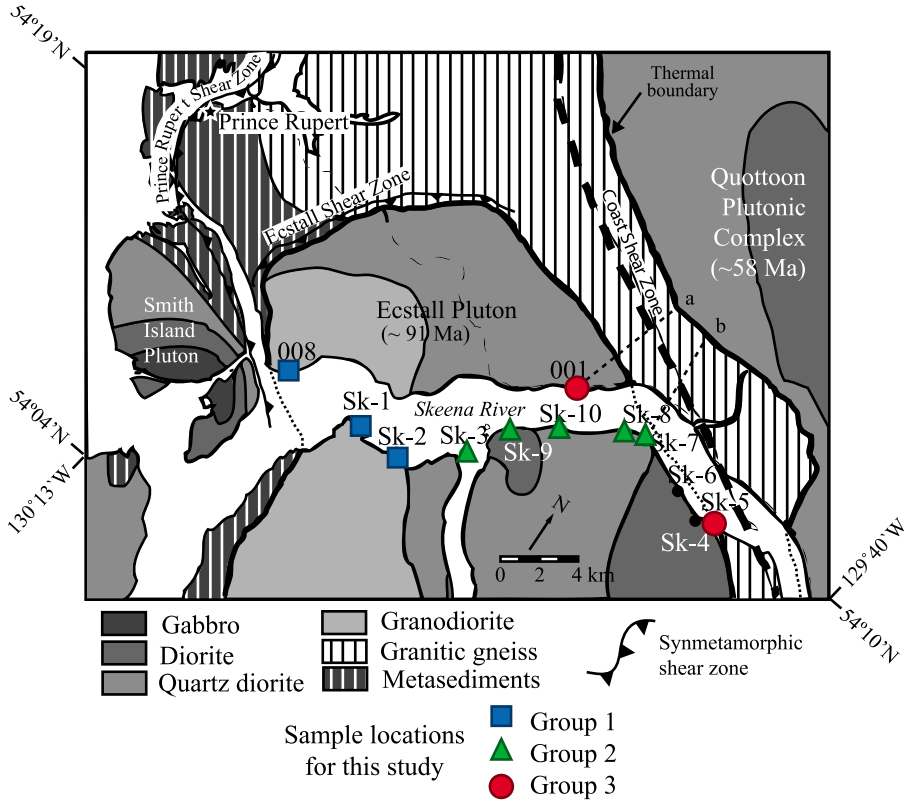

Figure 1. Generalized geologic map of the northern part of the Ecstall pluton from *Brownlee et al.* [2010]. Sample locations for single grain rock magnetic experiments in this study are indicated by colored symbols. Geologic relations are after *Hutchison* [1982], and structures are after *Butler et al.* [2002] and *Crawford et al.* [1987].

2.1. Rock Magnetic Measurements

2.1.1. Hysteresis

[6] Hysteresis loops were measured for at least three single Fe-Ti oxide grains from each sample, and when possible, each grain was measured in three orthogonal orientations. Hysteresis loops were collected using a Princeton Measurements Corporation alternating gradient magnetometer (AGM) at the Institute for Rock Magnetism at the University of Minnesota. First-order reversal curves (FORCs) were measured to determine the distribution of coercivities and magnetic interactions within each oxide grain [*Pike and Fernandez*, 1999; *Roberts et al.*, 2000]. FORC data was processed and analyzed using the FORCinel software [*Harrison and Feinberg*, 2008].

2.1.2. Low-Temperature Remanence Versus Temperature

[7] The low-temperature remanence of single Fe-Ti oxide grains was measured using a Quantum Design magnetic properties measurement system (MPMS) at the Institute for Rock Magnetism. Two styles of low-temperature remanence experiments were conducted. In the first, a room temperature–saturation isothermal remanent magnetization (RT-SIRM) was imparted using a 5 T field. The remanence of the sample was measured as temperature was cycled in 5 K steps to 10 K and then back to room temperature. The second style of experiment involved measurement of a 5 T SIRM imparted at 10 K after samples were cooled in either a 5 T field (field cooled; FC) or after zero-field cooling (ZFC). ZFC and FC remanence curves were measured during warming in 5 K steps from 10 K to room temperature. The low-temperature remanence of at least four single Fe-Ti oxide grains was measured for each group.

2.1.3. Room Temperature Isothermal Remanent Magnetization Acquisition

[8] Isothermal remanent magnetization (IRM) acquisition experiments were conducted at the Berkeley Geochronology Center using an ASC Scientific model IM-10-30 impulse magnetizer with a 5.1 cm diameter coil and a maximum applied field of 1.2 T. Remanence was measured using a 2G Enterprises

755R cryogenic magnetometer. To minimize the starting remanence, each grain was first demagnetized along three orthogonal axes using alternating fields up to 150 mT. Grains were then given a 1.2 T IRM and their remanence was measured in a stepwise fashion as progressively larger impulse fields were applied in an antipodal direction. At least four grains were measured from each group using ~40–60 steps. IRM acquisition curves were deconvolved into separate coercivity components using IRMunmixV2.2 by *Heslop et al.* [2002]. For consistency, all grains were modeled with four components using a spline fit with no smoothing, and no cropping, except for four grains that were cropped at the first point (i.e., all points except the first were used in the model fits).

2.2. Magnetic Imaging

[9] Images of magnetic domains within the ilmenite-hematite grains were collected at the Institute for Rock Magnetism using a Digital Instruments Nanoscope III magnetic force microscope (MFM). The MFM technique images stray magnetic fields that are perpendicular to a polished surface [*Martin and Wickramasinghe*, 1987]. Grains were mounted in epoxy and were polished to a 25 nm smoothness using colloidal silica. Additionally, Fe-Ti oxide grains in polished thin sections were imaged using a Digital Instruments Demension 3000.

[10] A complementary magnetic imaging technique, off-axis electron holography in a transmission electron microscope (TEM) was used at the University of Cambridge to study magnetic structures in the samples using the approach described by *Harrison et al.* [2002]. This technique allows the in-plane magnetic induction in minerals to be imaged quantitatively at the nanometer scale [*Feinberg et al.*, 2006; *Kasama et al.*, 2006; *Kasama et al.*, 2010]. Representative regions within oxide grains were transferred from thin sections onto TEM specimen Cu grids and were thinned to electron transparency by Ar ion milling. Each TEM specimen was coated with a thin layer of carbon to prevent charging. TEM observations were carried out at 300 kV using a Philips CM300-ST TEM equipped with a field emission gun, a Lorentz lens, an electrostatic biprism and a Gatan imaging filter. Digital acquisition and analysis of the electron holograms allowed the magnetic signal of primary interest to be separated from unwanted contributions to the contrast and mean inner potential from variations in specimen thickness [*Dunin-Borkowski et al.*, 2004]. Energy-selected imaging [*Egerton*, 1996; *Golla and Putnis*, 2001] was used to measure the compositions of the Fe-Ti oxide minerals present in each single crystal. Selected-area electron diffraction and dark field imaging were used to identify mineral phases and to investigate the distribution of mineral phases, respectively.

3. Results

[11] We discuss the magnetic properties of Fe-Ti oxides within the Ecstall pluton in terms of three groups that are related to the presence of specific internal microstructures (Table 1). Group 1 consists of samples that are >14 km from the thermal boundary at the Quottoon Plutonic complex (Figure 1). Group 1 oxides are finely exsolved grains of hematite and ilmenite with a limited range of microstructures. Ilmenite lamellae occur within hematite hosts, and lamella thicknesses are consistent between grains [*Brownlee et al.*, 2010]. Groups 2 and 3 consist of samples that are <14 km from the Quottoon Plutonic complex (Figure 1), and have been affected by reheating. In addition to the features described for group 1, both groups 2 and 3 contain magnetite within the hematite-ilmenite grains. Group 3 is distinguished from group 2 by the presence of a rutile blitz texture, which occurs in samples located <8 km from the Quottoon Plutonic complex.

3.1. Rock Magnetic Measurements

3.1.1. Hysteresis

[12] Due to the high coercivity of hematite, hysteresis experiments did not reach saturation for any sample (maximum field 1.8 T). Slope corrections were made using data collected at fields <1 T. To allow straightforward visual comparison between different samples, hysteresis loops were normalized to the magnetization at 1 T. There is a tendency for the loops not to close perfectly, which is a consequence of not reaching saturation.

[13] Hysteresis loops from group 1 are typical of hematite with coercivities >100mT [*Peters and Thompson*, 1998] (Figure 2a). The loops are relatively square with high M_r/M_s ratios, and have coercivities that range from ~150 to 250 mT. FORC diagrams from group 1 have coercivity distributions centered at ~150–200 mT, consistent with hematite (Figure 3a). The peak in the coercivity distribution is offset to negative H_u space, and is slightly curvilinear with a longer tail that extends to higher coercivities with more negative interactions. This type of distribution has been previously documented in natural hematite [*Muxworthy et al.*, 2005], but not

Table 1. Summary of Microstructures From *Brownlee et al.* [2010] Associated With Each Group and the General Shape of Hysteresis Loops From Each Group[a]

	Group 1	Group 2	Group 3
Microstructures (reflected light and SEM)	Dominantly hematite host grains with fine-scale (~1–5 μm) ilmenite exsolution lamellae. Few rutile needles.	Both hematite and ilmenite host grains. Large zones of ilmenite host within grains. Rutile needles are more common than in group 1. Pervasive alteration of ilmenite host zones.	Dominantly hematite host grains, but larger ilmenite host zones are present. Rutile blitz texture: abundant rutile cross-cutting ilemenite and hematite lamellae in six crystallographic orientations. Alteration of ilmenite zones.
Microstructures (TEM)	Fine exsolution lamellae (~10 nm) with coherent boundaries.	Fine exsolution lamellae (~10 nm). 20–50 nm size magnetite precipitates in hematite.	Fine exsolution lamellae (~10 nm). 20–50 nm size magnetite precipitates in hematite. Rutile blitz texture. Exsolved hematite in rutile.
Hysteresis loops	Square	Wasp-waisted	Both square and wasp-waisted

[a]Such as square or wasp-waisted.

Figure 2. Normalized hysteresis loops from the three sample groups. Saturation is not reached, therefore, slope corrections are made using the slope from ~500 –to 1000 mT, and hysteresis loops are normalized to the magnetization at 1 T. (a) Group 1, (b) group 2, and (c) group 3.

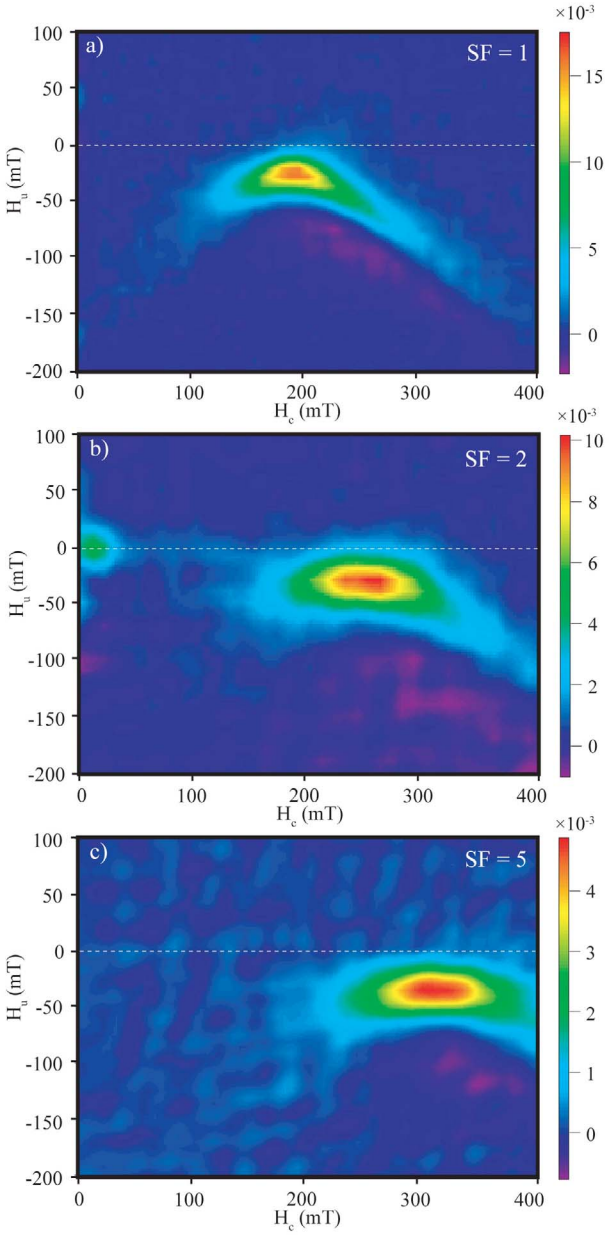

Figure 3. Representative FORC diagrams from the three sample groups calculated with FORCinel [*Harrison and Feinberg*, 2008] using the smoothing factors indicated. (a) Group 1, (b) group 2, and (c) group 3.

all hematite samples have the same kidney-shaped FORC distribution [*Pike and Fernandez*, 1999; *Roberts et al.*, 2006].

[14] Hysteresis loops from group 2 all have some degree of wasp-waistedness (Figure 2b), which can be interpreted as an indication of a mixture of two magnetic phases, in this instance, hematite and magnetite [*Roberts et al.*, 1995; *Tauxe et al.*, 1996]. There is significant variability in the degree of wasp-waistedness, which indicates heterogeneous proportions of magnetite in the different grains. Apparent coercivities range from 5 to 300 mT. FORC diagrams from group 2 have two coercivity peaks (Figure 3b), which correspond to hematite and magnetite. The magnetite peak is centered between 5 and 15 mT on the H_c axis, while the hematite peak is centered between 250 and 300 mT. The hematite peak from group 2 is again offset in the negative H_u direction as is the case for group 1 samples, although this offset appears to be slightly larger, and the mean FORC distribution is less kidney shaped.

[15] Group 3 hysteresis loops are also variable (Figure 2c). As is the case for group 2 samples, many have varying degrees of wasp-waistedness, but some hysteresis loops have no sign of magnetite. These single phase loops have the highest coercivities, ~350 to 400 mT. In FORC diagrams from single phase grains, the coercivity peak is again kidney shaped (Figure 3c), and is offset in the negative H_u direction. The negative offset is the largest in these grains, and the coercivity peak is wider and more flat than curvilinear.

3.1.2. Low-Temperature Remanence Versus Temperature

[16] Low-temperature remanence experiments for group 1 samples are not highly variable when normalized to the maximum remanence measured, which for all grains occurs at ~10 K in the FC experiments (Figure 4). Room temperature remanence is always between ~0.7 and ~0.85 of the SIRM at 10 K, and decreases upon cooling (Figure 4c). There is no definitive Morin transition in any of the group 1 samples, which is consistent with hematite containing significant Ti [*Ericsson et al.*, 1986]. There is a slight increase in remanence upon warming near 250 K, and then an equivalent decrease just above 250 K in a few samples. This bump only occurs upon warming, and only after cooling at least below 200 K. A similar bump is observed in one sample from *Dang et al.* [1998] that does not have a Morin transition, but its meaning is not discussed. This bump is most clearly seen in the FC and ZFC experiments. Additionally, the FC and ZFC results all indicate a strong remanence that is unblocked by ~40 K, which we attribute to magnetic relaxation in ilmenite [e.g., *Burton et al.*, 2008; *Dillon and Franke*, 2009].

[17] Low-temperature remanence experiments from group 2 samples have significant variability (Figure 4). Again the maximum remanence is found at ~10 K in the FC experiments. Room temperature remanence ranges from ~0.1 to ~0.45 of the maxi-

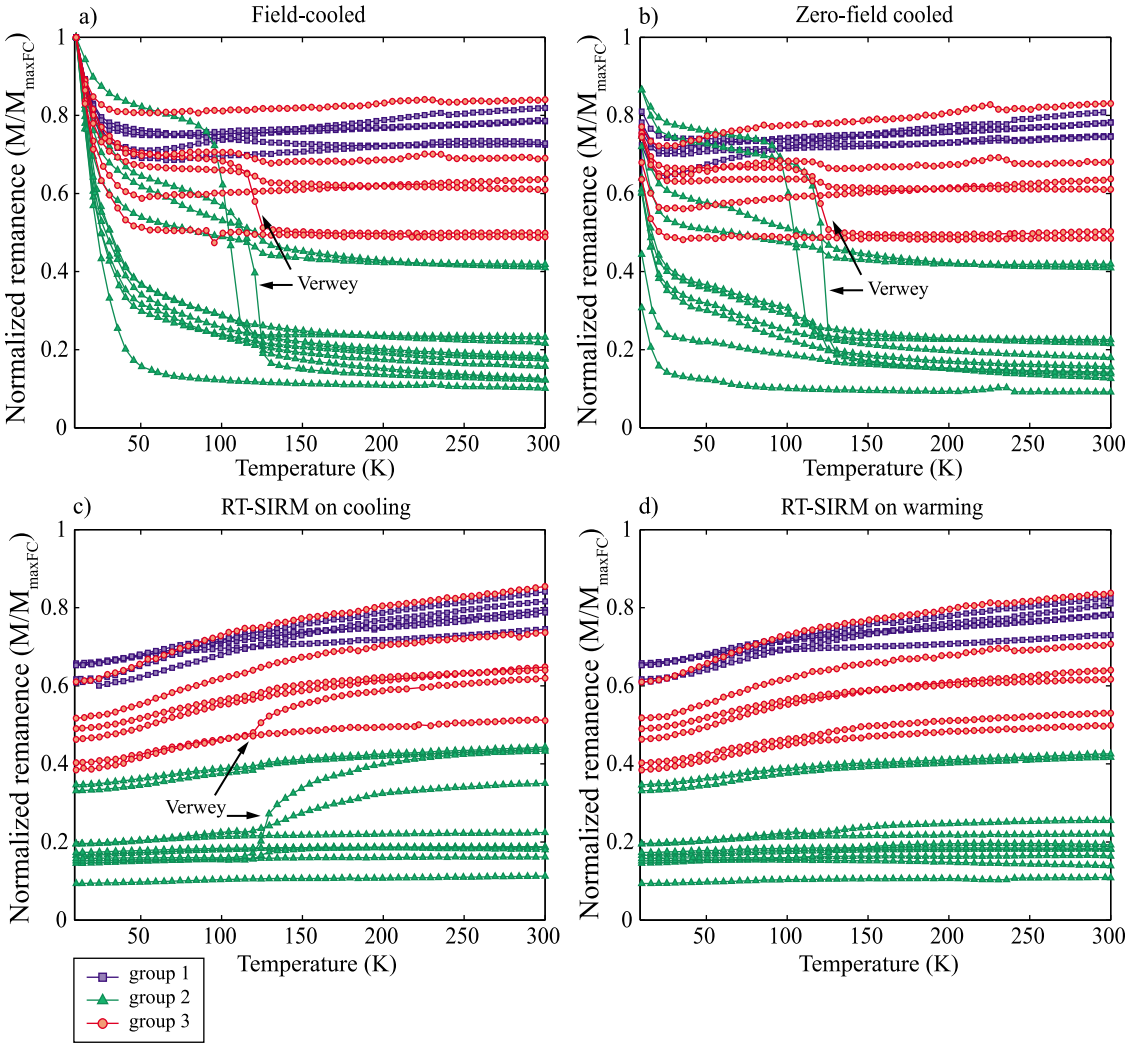

Figure 4. Low-temperature remanence versus temperature experiments. (a) Field-cooled remanence, (b) zero-field cooled remanence, (c) room temperature SIRM during cooling, and (d) room temperature SIRM during warming. Remanence measurements are normalized to the maximum measured for each grain, which occurs at ~10 K in the field-cooled experiment. Clear Verwey transitions are observed in samples from groups 2 and 3 in Figures 4a, 4b, and 4c.

mum, and is significantly lower than for group 1 samples. One grain exhibits the same behavior near 250 K as in the few grains from group 1 samples. Many grains have an unambiguous Verwey transition at ~110–120 K, which is attributed to the presence of magnetite [*Özdemir et al.*, 1993]. The range in observed Verwey transition temperatures indicates some degree of nonstoichiometry [*Özdemir et al*, 1993]. Group 2 grains also have a strong remanence associated with ilmenite that is unblocked by ~40 K.

[18] Low-temperature remanence experiments from group 3 samples have variability similar to group 2 samples (Figure 4). Maximum remanence occurs at ~10 K in the FC experiments. Room temperature remanences range from ~0.47 to ~0.85 of the maximum, which encompasses the range exhibited by group 1 samples, and is higher than that found in group 2 samples. Remanence perturbations are observed near 250 K, as seen in both group 1 and 2 samples. Many grains have a Verwey transition at ~120 K, which is attributed to varying amounts of stoichiometric magnetite. Remanence associated with ilmenite (unblocked by ~40 K) is less significant than in group 2 samples.

3.1.3. Room Temperature IRM Acquisition

[19] IRM acquisition experiments for group 1 samples are typical of hematite (i.e., coercivities >100 mT [*Peters and Thompson*, 1998; *Grygar*

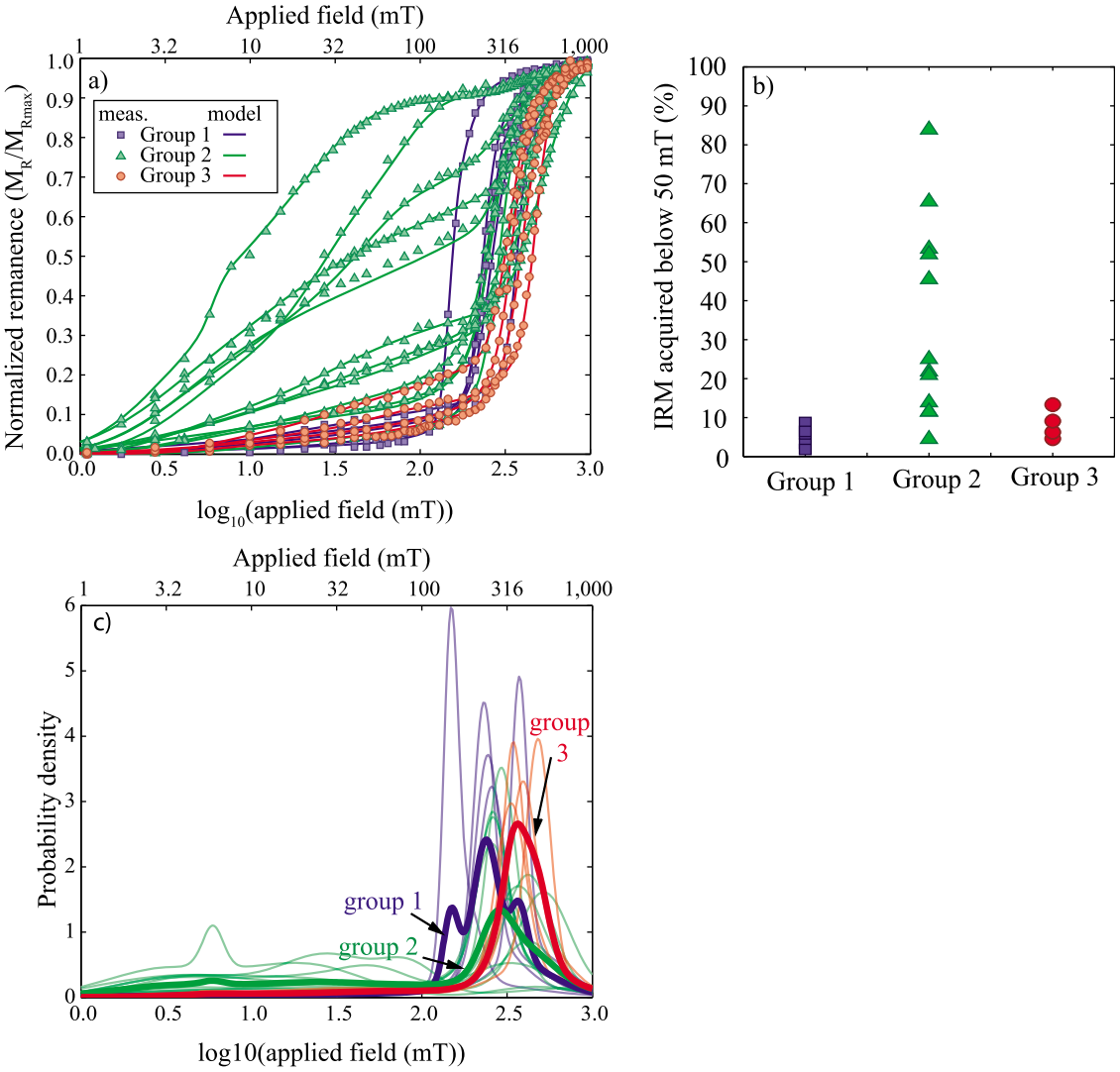

Figure 5. (a) IRM acquisition measurements (symbols) are fit by models (solid lines) with four components. Group 1 (blue squares) is dominated by phases with high coercivity, and groups 2 (green triangles) and 3 (red circles) have variable contributions from lower-coercivity phases that are consistent with magnetite. Saturation is not reached, therefore IRM curves are normalized to the remanence at 1.2 T (maximum applied field). (b) The percentage of the total IRM acquired below 50 mT is highest in group 2 samples. (c) The probability distribution curves for the models indicate that group 2 samples contain more low-coercivity components (magnetite) than group 3 samples and that there is a progression toward higher coercivities in group 3. Thin lines are models for each grain, and thick lines are the average of all grains for each group.

et al., 2003]) (Figure 5a). Less than 10% of the total IRM is acquired at fields below ~100 mT, after which remanence is acquired rapidly at 200 to 300 mT. Saturation is not achieved at 1200 mT, the maximum field that could be applied with our instrumentation. For consistency, all IRM acquisition curves are modeled using a total of four phases. IRM acquisition curves from group 1 samples are modeled well with up to four high-coercivity phases, which possibly reflect different hematite domain sizes. Four grains have a minimal (<6%) contribution from a low-coercivity phase consistent with magnetite (Table 2 and Figure 5).

[20] Group 2 IRM acquisition curves are suggestive of the presence of two magnetic phases, hematite and magnetite (Figure 5). Up to 90% of the IRM is acquired below 100 mT, which indicates a strong but varying contribution from magnetite. Saturation is not achieved at 1200 mT. IRM component fitting indicates the presence of two (in one instance three) low-coercivity phases, which are equivalent to

Table 2. Parameters of IRM Acquisition Models[a]

Phase	Contribution to IRM	B1/2	DP
	Group 1		
1	**1.01%**	**0.48**	**0.16**
2	17.56%	2.41	0.69
3	55.82%	2.36	0.06
4	25.61%	2.43	0.16
1	**5.79%**	**0.96**	**0.45**
2	10.81%	2.06	0.68
3	33.58%	2.64	0.20
4	49.81%	2.57	0.05
1	**3.44%**	**0.78**	**0.48**
2	8.01%	1.91	0.49
3	41.00%	2.55	0.22
4	47.55%	2.41	0.07
1	**4.47%**	**0.56**	**0.64**
2	9.26%	2.01	0.59
3	29.02%	2.51	0.20
4	57.25%	2.39	0.07
1	8.02%	2.40	1.45
2	13.33%	2.34	0.30
3	49.02%	2.17	0.04
4	29.63%	2.25	0.09
	Group 2		
1	**24.55%**	**0.53**	**0.34**
2	**22.72%**	**1.28**	**0.33**
3	20.50%	1.74	0.22
4	32.23%	2.52	0.25
1	**6.85%**	**0.46**	**0.50**
2	**8.90%**	**1.44**	**0.35**
3	38.45%	2.45	0.34
4	45.80%	2.41	0.10
1	**9.06%**	**0.75**	**0.42**
2	21.38%	2.44	0.61
3	31.35%	2.44	0.19
4	38.20%	2.42	0.08
1	**6.63%**	**0.70**	**0.40**
2	**7.40%**	**1.64**	**0.58**
3	38.05%	2.47	0.29
4	47.93%	2.42	0.09
1	**10.42%**	**0.57**	**0.49**
2	**11.35%**	**1.42**	**0.40**
3	27.26%	2.64	0.60
4	50.97%	2.57	0.14
1	**10.32%**	**0.68**	**0.50**
2	**8.39%**	**1.31**	**0.59**
3	23.50%	2.33	0.58
4	57.79%	2.62	0.14
1	**8.85%**	**0.55**	**0.30**
2	**16.20%**	**1.41**	**0.41**
3	22.46%	2.61	0.82
4	52.49%	2.72	0.15
1	**28.96%**	**0.50**	**0.40**
2	**18.54%**	**1.24**	**0.36**
3	30.15%	2.37	0.66
4	22.36%	2.63	0.13
1	**25.91%**	**0.66**	**0.34**
2	**42.73%**	**1.45**	**0.28**
3	17.05%	1.93	0.16
4	14.32%	2.94	0.41
1	**38.57%**	**0.50**	**0.35**
2	**9.84%**	**0.77**	**0.06**
3	**41.44%**	**1.32**	**0.34**
4	10.15%	2.68	0.25
1	**1.65%**	**0.90**	**0.32**
2	**6.02%**	**1.67**	**0.53**
3	31.47%	2.52	0.26
4	60.85%	2.47	0.08
1	**26.77%**	**0.58**	**0.36**
2	**16.90%**	**1.30**	**0.42**
3	24.90%	2.33	0.47
4	31.43%	2.51	0.10
	Group 3		
1	**1.57%**	**0.75**	**0.13**
2	**20.45%**	**1.59**	**0.59**
3	21.41%	2.62	0.28
4	56.57%	2.52	0.09
1	**3.05%**	**0.84**	**0.33**
2	9.90%	2.08	0.46
3	45.26%	2.64	0.19
4	41.79%	2.59	0.07
1	**8.51%**	**1.30**	**0.76**
2	18.40%	2.58	0.44
3	47.18%	2.56	0.12
4	25.90%	2.53	0.05
1	**6.78%**	**0.98**	**0.45**
2	6.03%	1.77	0.24
3	25.31%	2.63	0.23
4	61.88%	2.68	0.07

[a]Bold typeface indicates phases consistent with magnetite (B1/2 (log(mT))<1.7.

magnetite, and two (in one instance one) high-coercivity phases, which are equivalent to hematite (Table 2 and Figure 5).

[21] Group 3 IRM acquisition curves are also indicative of two magnetic phases, hematite and magnetite. In the four grains analyzed, up to 22% of the IRM was acquired below 100 mT. Saturation is not achieved at 1200 mT. Models of IRM acquisition include one (or two) low-coercivity phases that are consistent with the presence of magnetite, and three (or two) high-coercivity phases that are consistent with hematite (Table 2 and Figure 5). The high-coercivity phases in the group 3 samples have higher coercivities than those in group 1 and similar to slightly higher coercivities than the group 2 samples (Figure 5).

3.2. Magnetic Imaging

3.2.1. Magnetic Force Microscopy

[22] MFM imaging does not indicate a strong magnetic signal associated with exsolved ilmenite and hematite lamellae in any group of samples. Images from sample Sk-3 are shown in Figures 6 and 7.

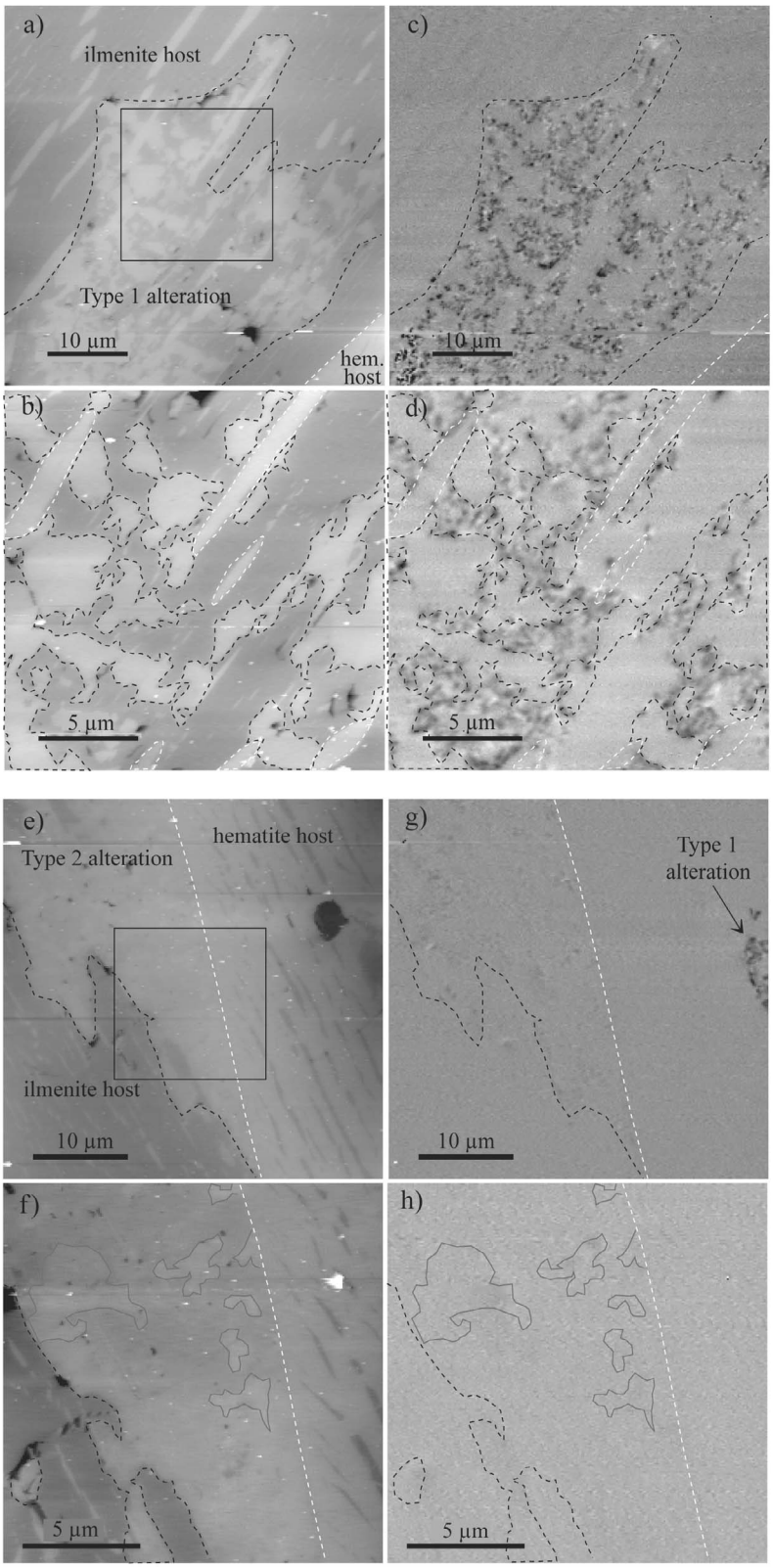
a)
ilmenite host
Type 1 alteration
10 μm
hem.
host
c)
10 μm
b)
5 μm
d)
5 μm
e)
hematite host
Type 2 alteration
ilmenite host
10 μm
g)
Type 1
alteration
10 μm
f)
5 μm
h)
5 μm

Figure 6

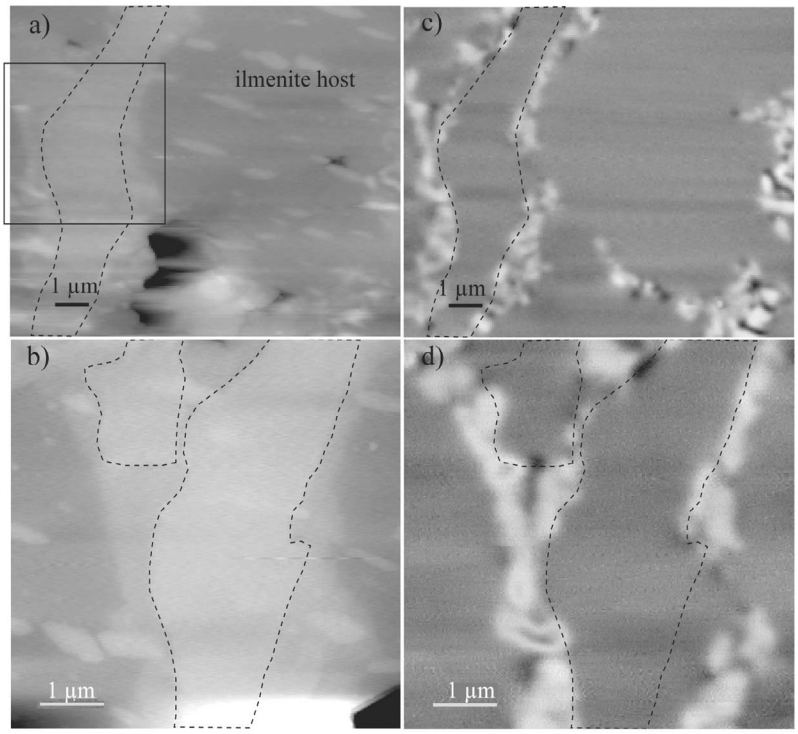

Figure 7. AFM and MFM images from sample Sk-3 in group 2, with magnetic signal outlining the edges of a phase that has the morphology of a kinked rutile needle. (a and b) AFM topographic image. The square in Figure 7a indicates the area of Figure 7b. (c and d) MFM phase or magnetic image. The brightest (highest) part of the alteration is outlined with a dashed black line.

Lamellae edges sometimes have weak magnetic signals, but these are not reproduced when the sample is rescanned after a 90° rotation, which indicates a strong topographic influence on the magnetic signal. There is, however, an observable magnetic signal in areas of altered ilmenite (Figure 6). Altered ilmenite is observed in samples from all three groups, but is very rare in group 1, which prevented us from analyzing this texture in any group 1 sample.

[23] Altered zones of ilmenite in samples from both groups 2 and 3 can be distinguished from unaltered ilmenite by their higher topography, and hence brighter appearance in AFM images. There are two variations in the appearance of altered ilmenite.

[24] Type 1 alteration occurs as patches of bright (higher topography) and dark (lower topography) regions (Figures 6a and 6b). The darker regions are indistinguishable in height from unaltered ilmenite. The darker regions have a strong magnetic signal. The magnetic signal appears to be due to randomly oriented dipoles, which we attribute to magnetite (Figures 6c and 6d). The magnetic particles are too small to be resolved in the MFM images. In a few cases, magnetite appears to have formed around a

Figure 6. Atomic force microscopy and magnetic force microscopy (AFM and MFM) images of the two types of ilmenite alteration from sample Sk-3 in group 2. (a and b) AFM topographic images of type 1 ilmenite alteration (see text for descriptions of type 1 and type 2 alteration). Brighter grays correspond to higher topography. The square in Figure 6a indicates the area of Figure 6b. (c and d) MFM phase or magnetic image from Figures 6a and 6b, respectively. There is no significant magnetic signal from the unaltered ilmenite regions (Figures 6a and 6c, upper left-hand corner). The magnetic signal is coming from the areas around the brighter patches in the altered areas. For reference in Figures 6b and 6d, larger hematite lamellae are outlined in dashed white lines, and bright alteration patches are outlined in dashed black lines. (e and f) AFM topographic images of type 2 ilmenite alteration. The square in Figure 6e indicates the area of Figure 6f. The dashed white line indicates the boundary between ilmenite and hematite host zones, and the dashed black line outlines type 2 alteration in ilmenite. A few of the apparent brighter patches in Figure 6f are outlined in gray. (g and h) MFM phase or magnetic image of type 2 alteration. This alteration has only a faint magnetic signal compared with that from type 1 alteration.

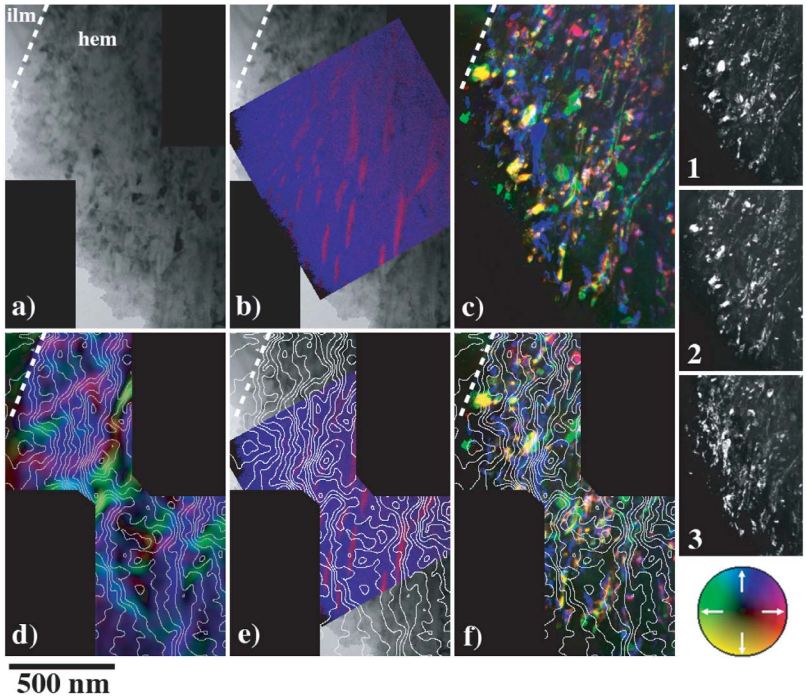

Figure 8. Summary of off-axis electron holography. (a) Bright field image and (b) corresponding elemental map of a single hematite lamella from sample Sk-3 in group 2; red denotes Ti, and blue denotes Fe. Ilmenite lamellae appear within the hematite host as red linear features in the elemental map but are obscured in the bright field image by the mottling associated with the magnetite precipitates. (c) Combined dark field images that highlight magnetite precipitates; yellow denotes image 1, red denotes image 2, and blue denotes image 3. (d) Color induction map with contours of magnetic induction. Contour spacing is 0.25 radians. Colors correspond to directions indicated by the color wheel. Induction is strongest where contours are closest together. (e) Magnetic induction contours overlain on the elemental map from Figure 8b. Induction is strongest in hematite just outside of ilmenite lamellae. (f) Magnetic induction contours overlain on the combined dark field image from Figure 8c. Areas of high induction correspond with magnetite precipitates.

phase with a morphology similar to a kinked rutile needle (Figure 7).

[25] Type 2 alteration is similar to type 1, but the darker regions no longer have the same height as unaltered ilmenite. All of the alteration products have higher topography, and patches, although still visible, are much less obvious. Little magnetic signal originates from these alteration regions, although they do appear to be slightly more magnetic than the unaltered ilmenite (Figure 6).

3.2.2. Off-Axis Electron Holography

[26] Off-axis electron holography investigation of one Fe-Ti oxide grain from sample Sk-3 (group 2), which includes magnetite precipitates, revealed that there was a measurable, thermally stable magnetic signal from the hematite regions that contain a significant amount of magnetite. The holograms were acquired in zero applied field, and are therefore a measure of remanence magnetization. The area investigated by holography was altered hematite, whereas the region investigated using MFM was altered ilmenite. In this region, lamellar magnetism at the interface between ilmenite and hematite, as proposed by *Robinson et al.* [2002], is unlikely because most of the hematite host is altered to magnetite. Even if lamellar magnetizations exist at the interfaces, the magnetization would be about 25 times weaker than the measured magnetizations, according to calculations based on the work by *Kasama et al.* [2009]. Therefore, although we cannot exclude the possible presence of lamellar magnetism, the measured magnetic signal is mostly due to magnetite. When magnetic induction contours are viewed over dark field images that highlight the magnetite precipitates, there is a correlation between areas with strong magnetic signal and magnetite precipitates (Figure 8). However, because the magnetite precipitates are randomly oriented, they are not all apparent in a single dark field image. The three areas containing ⟨111⟩ and ⟨220⟩ crystallographic reflections in the electron diffraction pattern have been used to generate a combined dark field

image in Figure 8c to highlight as many magnetite precipitates as possible. It is possible that not all of the magnetite precipitates have been imaged, and a small degree of mismatch may be expected between the holograms and dark field images owing to the lack of clear features to match. Regardless, correlation between the strong magnetic signal and magnetite precipitates is more clearly visible using the combined dark field image. Some of the highlighted particles may be associated with altered hematite or unknown iron minerals, although many particles are magnetite. Some magnetite crystals do not have strong magnetic signals, which might be related to the crystals being oriented such that they have significant out-of-plane components of magnetization, or complicated magnetic coupling through the specimen thickness or unknown nonmagnetic phases. Regions with strong magnetic signals that are not highlighted could be due to magnetite crystals that are oriented such that they are not highlighted in the dark field images.

4. Discussion

[27] Rock magnetic properties of single Fe-Ti oxide grains from the Ecstall pluton correlate well with the microstructural properties and proximity to the thermal boundary associated with the Quotoon plutonic complex. The magnetic properties of grains from group 1, which are furthest from the thermal boundary and unaffected by reheating, are dominated by hematite. There is some rock magnetic variability within group 1, but much less than that observed in either groups 2 or 3. This is consistent with observations from optical microscopy, SEM, and TEM of Fe-Ti oxides from this part of the Ecstall pluton, which indicate that the grains are primarily hematite with fine-scale ilmenite lamellae and little variation in appearance among grains [*Brownlee et al.*, 2010]. In summary, the magnetic properties of the unheated part of Ecstall pluton are relatively homogeneous.

[28] In contrast, grains from groups 2 and 3, which are closer to the thermal boundary and hence more affected by reheating, have significant variations in rock magnetic properties that relate to varying abundances of magnetite and ilmenite. The relative contribution of ilmenite can be seen in the low-temperature remanence experiments. Ilmenite with some Fe^{+3} enters a spin glass state below about 40 K, which allows it to acquire a strong remanence when cooled below this temperature in a 5 T field [*Burton et al.*, 2008]. For all grains from groups 2 and 3, the strongest remanence is observed at ~10 K in FC experiments. The relative difference between the room temperature remanence held by hematite and magnetite, and the remanence at ~10 K held mostly by ilmenite and magnetite, is an indication of the relative amounts of hematite and ilmenite. The relative contribution from magnetite at low temperatures can be inferred from the remanence below the Verwey transition and above 40 K. Samples from group 2 have room temperature remanence between 10 and 50% of the remanence at ~10 K, which indicates a high contribution from ilmenite and/or magnetite. Observations from optical microscopy and SEM analyses indicate that Fe-Ti oxides from groups 2 and 3 have more ilmenite than those in group 1 [*Brownlee et al.*, 2010]. The room temperature remanence of group 3 samples is between 50 and 80% of the remanence at 10 K. The contribution from ilmenite appears to be slightly less in group 3 than in group 2, but slightly more than in group 1.

[29] Using a few simplifying assumptions, the relative contributions of each phase to the low-temperature remanence in the FC experiment can be deconvolved, and are plotted as a ternary diagram in Figure 9. The assumptions are as follows: (1) the remanence at 10 K is from all three phases, hematite + ilmenite + magnetite; (2) the remanence below the Verwey transition and above 40 K (from ~50 to 100 K) is from magnetite + hematite; and (3) the room temperature remanence after warming is from hematite. While this is an oversimplification, the assumptions produce results consistent with observations from microscopy and IRM acquisition experiments. Namely, group 1 grains are dominantly hematite with ilmenite lamellae; groups 2 and 3 have greater contributions from magnetite and are pulled toward the magnetite end of the ternary diagram; and group 2 has on average more magnetite than group 3, and generally more ilmenite than hematite. Group 3 populates the ternary space between groups 1 and 2, and has hematite-ilmenite-magnetite compositions that could be formed by oxidizing the magnetite in group 2 samples back to hematite.

[30] Group 3 is distinguished from group 2 by the presence of rutile blitz texture. Although rutile is diamagnetic and is therefore not expected to affect hysteresis parameters, there are systematic differences between the two groups. Group 3 has higher average coercivities and reduced concentrations of magnetite. The higher coercivities may be caused by two distinct processes. The first involves further fine-scale exsolution of ilmenite and hematite. These Fe-Ti oxides grains experienced reheating above the miscibility gap of ilmenite-hematite (~390°C [*Ghiorso and Evans*, 2008]), which allows

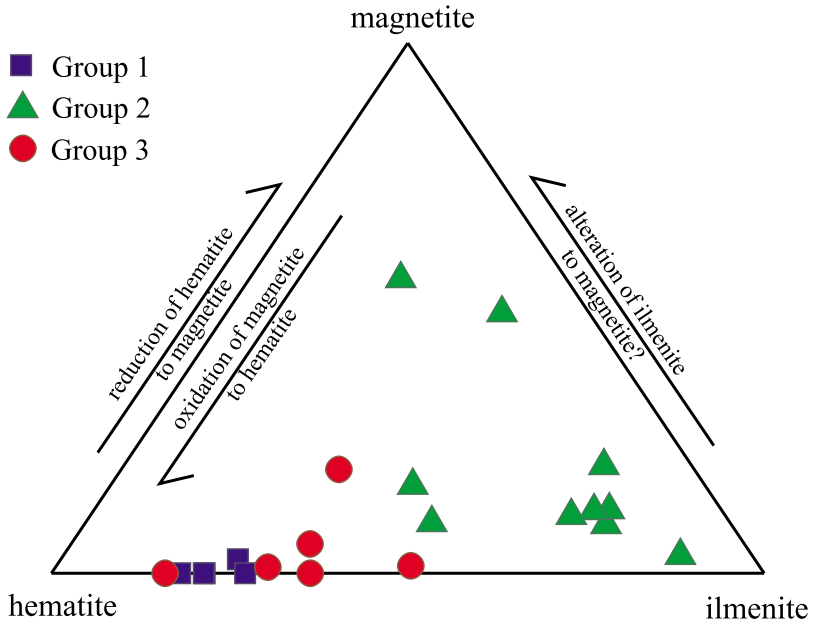

Figure 9. Ternary plot of the hematite-ilmenite-magnetite composition of oxide grains based on assumptions and field-cooled remanence experiments. Group 1 (blue squares) has the least variability and is dominated by hematite. Groups 2 (green triangles) and 3 (red circles) have greater variability, with more magnetite than group 1. Group 2 has the most magnetite and ilmenite. Arrows indicate trajectories that the composition would follow for each reaction. Assumptions: normalized magnetization, M_N (300 K) = hematite; M_N (50–100 K) = hematite + magnetite (if M_N (50–100 K) < M_N (300 K) then zero contribution from magnetite is assumed); and M_N (10 K) = hematite + magnetite + ilmenite.

for further exsolution upon cooling. The presence of more fine-scale lamellae will lead to higher coercivities due to the effect of lamellar magnetism [*Robinson et al.*, 2006]. The second process responsible for higher coercivity is exsolution of hematite from rutile. Fine hematite precipitates are seen in TEM images of the large rutile needles that make up the blitz textures within these grains [*Brownlee et al.*, 2010]. While the magnetic properties of rutile with fine hematite precipitates have not been studied in detail, high coercivity may be expected due to the small size and high shape anisotropy of the hematite precipitates.

[31] Both groups 2 and 3 contain magnetite that formed during reheating of the Ecstall pluton. On average, grains within group 3 contain less magnetite per unit volume than those within group 2. The occurrence of magnetite and hematite together in the same mineral grain produces hysteresis loops with a certain degree of wasp-waistedness, the degree of which is proportional to the concentration of magnetite [*Roberts et al.*, 1995; *Tauxe et al.*, 1996]. Magnetite forms as a product of two separate processes within these grains: (1) reduction of hematite [*Brownlee et al.*, 2010] and (2) alteration of ilmenite as seen in MFM imaging. Evidence for hematite transformation to magnetite via reduction is presented in the work by *Brownlee et al.* [2010], and it is argued that hematite was subjected to a T-fO_2 environment within the magnetite stability field during rapid reheating by the Quotoon Plutonic Complex. As the reheated portion of the Ecstall pluton cooled, T-fO_2 conditions returned to the hematite stability field, whereupon a fraction of the newly produced magnetite was oxidized back to hematite. Portions of the Ecstall pluton closest to the Quotoon Pluton would have cooled more slowly, thereby allowing a larger fraction of the magnetite to be oxidized back to hematite.

[32] MFM observations of magnetite within zones of ilmenite alteration are more problematic to explain. Ilmenite alteration is typically associated with oxidation, and while laboratory studies of ilmenite oxidation have revealed numerous reactions involving a complex variety of stable and metastable phases (hematite, rutile, pseudobrookite, brookite, and anatase), none of these reactions predict the occurrence of magnetite [*Frost et al.*, 1986; *Briggs and Sacco*, 1993]. However, laboratory-induced reduction of ilmenite commonly produces metallic iron and reduced oxides in the form of Ti_nO_{2n-1} and $(Fe,Ti)_3O_5$ [*Grey et al.*, 1973; *Gupta et al.*, 1987]. Generation of hematite in strongly oxidizing environments and metallic iron in strongly

reducing environments suggests that a range of iron oxide compositions may be produced during ilmenite alteration. Given that T-fO_2 conditions within the Ecstall pluton were reducing enough to be amenable to magnetite formation via hematite, it seems feasible that portions of ilmenite have also been transformed (directly or indirectly) into magnetite.

[33] Magnetite grains within zones of ilmenite alteration appear to be situated around the edges of a second nonmagnetic phase, which in some instances has a morphology similar to that of a kinked rutile needle, such as would be observed in blitz textures. Rutile is a common product of ilmenite alteration [*Frost et al.*, 1986].

[34] The amount of hematite relative to ilmenite varies between grains, as can be seen in light microscope and SEM images [*Brownlee et al.*, 2010]. The ilmenite alteration is heterogeneous, even within grains [*Brownlee et al.*, 2010], and furthermore, not all ilmenite alteration produces magnetite. Since both sources of magnetite are expected to vary between grains, it is not surprising that the magnetic properties associated with magnetite have the same degree of variability.

[35] Finally, fluids may have played an important role in both oxidation and reduction in these oxide grains. Although there is no obvious evidence of fluid interaction within the grains (i.e., alteration associated with cracks), we cannot discount the possibility that fluids may have influenced the final magnetic mineral assemblage. A study specifically aimed at the role of fluids in formation of the Fe-Ti oxides of the Ecstall pluton may look at the oxygen isotope composition of Fe-Ti oxides in relation to distance from the Quottoon Pluton. It would also be interesting to compare the isotopic composition of rutile in the Fe-Ti oxides of group 2 samples, which do not have blitz texture, with the rutile that makes up the blitz texture in group 3 samples.

5. Conclusions

[36] Rock magnetic properties of single crystals of ilmenite-hematite from the Ecstall pluton can be divided into three groups that correspond to microstructures documented by *Brownlee et al.* [2010]. The groups vary with distance from the Quottoon Plutonic Complex, which was responsible for reheating the locations from which samples from both groups 2 and 3 were recovered. The spatial distribution of groupings reveals two important things. First, magnetic properties of grains from group 1, >14 km from the Quottoon Pluton, are different than those from groups 2 or 3 which suggests that reheating has affected the magnetic properties of the Fe-Ti oxides in groups 2 and 3. Second, the magnetic properties that distinguish groups 2 and 3 reflect changes in mineral microstructures, which in turn are related by their distance from the thermal boundary.

[37] The occurrence of magnetite in both group 2 and 3 grains has a profound effect on the magnetic properties of these Fe-Ti oxides. Magnetite exists in two places within these grains, as a product of hematite reduction [*Brownlee et al.*, 2010], and a product of ilmenite alteration. The suite of rock magnetic experiments reported here is unable to distinguish between the two types of magnetite, although a more detailed examination of the coercivity distributions within these grains may allow this level of differentiation in the future.

[38] The results from this study indicate that the shallow paleomagnetic inclinations in the western part of the Ecstall pluton should record a magnetization related to the original emplacement of the Ecstall pluton. In the absence of postmagnetization deformation, these shallow inclinations are consistent with the most extreme estimates of northward translation associated with the Baja-BC hypothesis. $^{40}Ar/^{39}Ar$ geochronology and thermal modeling suggest that the Ecstall pluton experienced northeast up tilting as well as reheating [*Brownlee and Renne*, 2010]. Correcting the paleomagnetic directions in the western part of the Ecstall pluton for tilting in this sense will increase the inclinations, and decrease the suggested translations. If the postmagnetization deformation history of the Ecstall pluton, and other deeply seated plutons in western BC, can be better constrained, then more reliable estimates of paleolatitude may be obtained. In addition to deformation, future paleomagnetic studies in this area must consider the effects of secondary reheating on microstructures of magnetic minerals, which also affects the paleomagnetic directions recorded in these rocks.

Acknowledgments

[39] This work was funded by two IRM visiting fellowships, NSF grant EAR-0440029 and NERC grant NE/D002036/1. We thank Mike Jackson, Peat Solheid, and Julie Bowles at the IRM; Ken Verosub at UC Davis; Lincoln Hollister for help and encouragement along the way; Lisa Smeenk for assistance

in the BGC paleomagnetic lab; and Courtney Hart and Peter Freeman for fieldwork assistance. This manuscript was improved by constructive reviews from Bernie Housen, an anonymous reviewer, and Editor Andrew Roberts.

References

Beck, M. E., Jr., and B. A. Housen (2005), Comment on "Paleomagnetism and geochronology of the Ecstall pluton in the Coast Mountains of British Columbia: Evidence for local deformation rather than large-scale transport" by R. F. Butler et al., *J. Geophys. Res.*, *110*, B01101, doi:10.1029/2004JB003346.

Briggs, R. A., and A. Sacco (1993), The oxidation of ilmenite and it's relationship to the FeO-Fe2O3-TiO2 phase diagram at 1073-K and 1140-K, *Metall. Trans. A*, *24*, 1257–1264, doi:10.1007/BF02668194.

Brownlee, S. J., and P. R. Renne (2010), Thermal history of the Ecstall pluton from $^{40}Ar/^{39}Ar$ geochronology and thermal modeling, *Geochim. Cosmochim. Acta*, *74*, 4375–4391, doi:10.1016/j.gca.2010.04.023.

Brownlee, S. J., J. M. Feinberg, R. J. Harrison, T. Kasama, G. R. Scott, and P. R. Renne (2010), Effects of temperature on ilmenite-hematite: Microstructure and magnetic properties in the Ecstall pluton, British Columbia, *Am. Mineral.*, *95*, 153–160, doi:10.2138/am.2010.3191.

Burton, B. P., P. Robinson, S. A. McEnroe, K. Fabian, and T. B. Ballaran (2008), A low-temperature phase diagram for ilmenite-rich compositions in the system Fe_2O_3-$FeTiO_3$, *Am. Mineral.*, *93*, 1260–1272, doi:10.2138/am.2008.2690.

Butler, R. F., G. E. Gehrels, S. L. Baldwin, and C. Davidson (2002), Paleomagnetism and geochronology of the Ecstall pluton in the Coast Mountains of British Columbia: Evidence for local deformation rather than large-scale transport, *J. Geophys. Res.*, *107*(B1), 2009, doi:10.1029/2001JB000270.

Cowan, D. S., M. T. Brandon, and J. I. Garver (1997), Geologic tests of hypotheses for large coastwise displacements: A critique illustrated by the Baja British Columbia controversy, *Am. J. Sci.*, *297*, 117–173, doi:10.2475/ajs.297.2.117.

Crawford, M. L., L. S. Hollister, and G. J. Woodsworth (1987), Crustal deformation and regional metamorphism across a terrane boundary, Coast Plutonic Complex, British Columbia, *Tectonics*, *6*, 343–361, doi:10.1029/TC006i003p00343.

Dang, M.-Z., D. G. Rancourt, J. E. Dutrizac, G. Lamarche, and R. Provencher (1998), Interplay of surface conditions, particle size, stoichiometry, cell parameters, and magnetism in sunthetic hematite-like materials, *Hyperfine Interact.*, *117*, 271–319.

Dillon, M., and C. Franke (2009), Diagenetic alteration of natural Fe-Ti oxides identified by energy dispersive spectroscopy and low-temperature remanence and hysteresis measurements, *Phys. Earth Planet. Inter.*, *172*, 141–156, doi:10.1016/j.pepi.2008.08.003.

Dunin-Borkowski, R. E., M. R. McCartney, and D. J. Smith (2004), Electron holography of nanostructured materials, in *Encyclopedia of Nanoscience and Nanotechnology*, edited by H. S. Nalwa, pp. 41–99, Am. Sci., Stevenson Ranch, Calif.

Egerton, R. F. (1996), *Electron Energy-Loss Spectroscopy in the Electron Microscope*, 2nd ed., Plenum Press, New York.

Enkin, R. J., J. B. Mahoney, J. Baker, J. Riesterer, and M. L. Haskin (2003), Deciphering shallow paleomagnetic inclinations: 2. Implications from Late Cretaceous strata overlapping the Insular/Intermontane Superterrane boundary in the southern Canadian Cordillera, *J. Geophys. Res.*, *108*(B4), 2186, doi:10.1029/2002JB001983.

Ericsson, T., A. Krishnamurthy, and B. K. Srivastava (1986), Morin-transition in Ti-substituted hematite–A Mossbauer study, *Phys. Scr.*, *33*, 88–90, doi:10.1088/0031-8949/33/1/013.

Feinberg, J. M., R. J. Harrison, T. Kasama, R. E. Dunin-Borkowski, G. R. Scott, and P. R. Renne (2006), Effects of internal mineral structures on the magnetic remanence of silicate-hosted titanomagnetite inclusions: An electron holography study, *J. Geophys. Res.*, *111*, B12S15, doi:10.1029/2006JB004498.

Frost, M. T., I. E. Grey, I. R. Harrowfield, and C. Li (1986), Alteration profiles and impurity element distributions in magnetic fractions of weathered ilmenite, *Am. Mineral.*, *71*, 167–175.

Ghiorso, M. S., and B. W. Evans (2008), Thermodynamics of rhombohedral oxide solid solutions and a revision of the Fe-Ti two-oxide geothermometer and oxygen-barometer, *Am. J. Sci.*, *308*, 957–1039, doi:10.2475/09.2008.01.

Golla, U., and A. Putnis (2001), Valence state mapping and quantitative electron spectroscopic imaging of exsolution in titanohematite by energy-filtered TEM, *Phys. Chem. Miner.*, *28*, 119–129, doi:10.1007/s002690000136.

Grey, I. E., D. G. Jones, and A. F. Reid (1973), Reaction sequences in the reduction of ilmenite, *Trans. Inst. Min. Metall., Sect. C*, *83*, 39–46.

Grygar, T., J. Dedecek, P. P. Kruiver, M. J. Dekkers, P. Bezdicka, and O. Schneeweiss (2003), Iron oxide mineralogy in late Miocene red beds from La Gloria, Spain: Rock-magnetic, voltammetric and Vis spectroscopy analyses, *Catena*, *53*, 115–132.

Gupta, S. K., V. Rajakumar, and P. Grieveson (1987), Kinetics of reduction of ilmenite with graphite at 1000 to 1100°C, *Trans. Inst. Min. Metall., Sect. B*, *18*, 713–718, doi:10.1007/BF02672888.

Harrison, R. J., and J. M. Feinberg (2008), FORCinel: An improved algorithm for calculating first-order reversal curve (FORC) distributions using locally weighted regression smoothing, *Geochem. Geophys. Geosyst.*, *9*, Q05016, doi:10.1029/2008GC001987.

Harrison, R. J., R. E. Dunin-Borkowski, and A. Putnis (2002), Direct imaging of nanoscale magnetic interactions in minerals, *Proc. Natl. Acad. Sci. U. S. A.*, *99*, 16,556–16,561, doi:10.1073/pnas.262514499.

Heslop, D., M. J. Dekkers, P. P. Kruiver, and I. H. M. Van Oorschot (2002), Analysis of isothermal remanent magnetization acquisition curves using the expectation-maximization algorithm, *Geophys. J. Int.*, *148*, 58–64, doi:10.1046/j.0956-540x.2001.01558.x.

Hollister, L. S., R. B. Hargraves, T. S. James, and P. R. Renne (2004), The paleomagnetic effects of reheating the Ecstall pluton, British Colombia, *Earth Planet. Sci. Lett.*, *221*, 397–407, doi:10.1016/S0012-821X(04)00067-6.

Hutchison, W. W. (1982), Geology of the Prince Rupert-Skeena map area, British Columbia, *Mem. Geol. Surv. Can.*, *394*, 116 pp.

Kasama, T., M. Posfai, R. K. K. Chong, A. P. Finlayson, P. R. Buseck, R. B. Frankel, and R. E. Dunin-Borkowski (2006), Magnetic properties, microstructure, composition, and morphology of greigite nanocrystals in magnetotactic bacteria from electron holography and tomography, *Am. Mineral.*, *91*, 1216–1229, doi:10.2138/am.2006.2227.

Kasama, T., R. E. Dunin-Borkowski, T. Asaka, R. J. Harrison, R. K. K. Chong, S. A. McEnroe, E. T. Simpson, Y. Matsui, and A. Putnis (2009), The application of Lorentz transmission electron microscopy to the study of lamellar magnetism in hematite-ilmenite, *Am. Mineral.*, *94*, 262–269, doi:10.2138/am.2009.2989.

Kasama, T., N. S. Church, J. M. Feinberg, R. E. Dunin-Borkowski, and R. J. Harrison (2010), Direct observation of ferromagnetic.ferroelastic domain interactions in magnetite below the Verwey transition, *Earth Planet. Sci. Lett.*, *297*, 10–17, doi:10.1016/j.epsl.2010.05.004.

Martin, Y., and H. K. Wickramasinghe (1987), Magnetic imaging by "force microscopy" with 1000 Å resolution, *Appl. Phys. Lett.*, *50*, 1455–1457, doi:10.1063/1.97800.

Muxworthy, A. R., J. G. King, and D. Heslop (2005), Assessing the ability of first-order reversal curve (FORC) diagrams to unravel complex magnetic signals, *J. Geophys. Res.*, *110*, B01105, doi:10.1029/2004JB003195.

Özdemir, Ö., D. J. Dunlop, and B. M. Moskowitz (1993), The effect of oxidation on the Verwey transition in magnetite, *Geophys. Res. Lett.*, *20*, 1671–1674.

Peters, C., and R. Thompson (1998), Magnetic identification of selected natural iron oxides and sulphides, *J. Magn. Magn. Mater.*, *183*, 365–374, doi:10.1016/S0304-8853(97)01097-4.

Pike, C., and A. Fernandez (1999), An investigation of magnetic reversal in submicron-scale dots using first order reversal curve diagrams, *J. Appl. Phys.*, *85*, 6668–6676, doi:10.1063/1.370177.

Roberts, A. P., Y. Cui, and K. L. Verosub (1995), Wasp-waisted hysteresis loops: Mineral magnetic characteristics and discrimination of components in mixed magnetic systems, *J. Geophys. Res.*, *100*, 17,909–17,924, doi:10.1029/95JB00672.

Roberts, A. P., C. R. Pike, and K. L. Verosub (2000), First-order reversal curve diagrams: A new tool for characterizing the magnetic properties of natural samples, *J. Geophys. Res.*, *105*, 28,461–28,475, doi:10.1029/2000JB900326.

Roberts, A. P., Q. Liu, C. J. Rowan, L. Chang, C. Carvallo, J. Torrent, and C.-S. Horng (2006), Characterization of hematite (α-Fe_2O_3), goethite (α-FeOOH), greigite (Fe_3S_4), and pyrrhotite (Fe_7S_8) using first-order reversal curve diagrams, *J. Geophys. Res.*, *111*, B12S35, doi:10.1029/2006JB004715.

Robinson, P., R. J. Harrison, S. A. McEnroe, and R. B. Harvgraves (2002), Lamellar magnetism in the haematite-ilmenite series as an explanation for strong remanent magnetization, *Nature*, *418*, 517–520, doi:10.1038/nature00942.

Robinson, P., F. Heidelbach, A. M. Hirt, S. A. McEnroe, and L. L. Brown (2006), Crystallographic-magnetic correlations in single-crystal haemo-ilmenite: New evidence for lamellar magnetism, *Geophys. J. Int.*, *165*, 17–31, doi:10.1111/j.1365-246X.2006.02849.x.

Tauxe, L., T. A. T. Mullender, and T. Pick (1996), Potbellies, wasp-waists, and superparamagnetism in magnetic hysteresis, *J. Geophys. Res.*, *101*, 571–583, doi:10.1029/95JB03041.

Umhoefer, P. J. (1987), Northward translation of "Baja British Columbia" along the late Cretaceous to Paleocene margin of western North America, *Tectonics*, *6*, 377–394, doi:10.1029/TC006i004p00377.

Wynne, P., E. Irving, J. Maxson, and K. Kleinspehn (1995), Paleomagnetism of the Upper Cretaceous strata of Mount Tatlow: Evidence for 3000 km of northward displacement of the eastern Coast Belt, British Columbia, *J. Geophys. Res.*, *100*, 6073–6091.